Validation of the dynamic wake meander model for loads and power production in the Egmond aan Zee wind farm

Larsen, Torben J.; Aagaard Madsen , Helge; Larsen, Gunner Chr.; Hansen, Kurt Schaldemose

Published in:
Wind Energy

Link to article, DOI:
10.1002/we.1563

Publication date:
2013

Document Version
Publisher's PDF, also known as Version of record

Wind Energy

WIND ENERGY
Wind Energ. (2012)
Published online in Wiley Online Library (wileyonlinelibrary.com). DOI: 10.1002/we.1563

RESEARCH ARTICLE

Validation of the dynamic wake meander model for loads and power production in the Egmond aan Zee wind farm

Torben J. Larsen, Helge Aa. Madsen, Gunner C. Larsen and Kurt S. Hansen

Technical University of Denmark, Wind Energy Division, Building 118, PO Box 49, 4000 Roskilde, Denmark

ABSTRACT

This paper investigates wake effects on load and power production by using the dynamic wake meander (DWM) model implemented in the aeroelastic code HAWC2. The instationary wind farm flow characteristics are modeled by treating the wind turbine wakes as passive tracers transported downstream using a meandering process driven by the low frequent cross-wind turbulence components. The model complex is validated by comparing simulated and measured loads for the Dutch Egmond aan Zee wind farm consisting of 36 Vestas V90 turbine located outside the coast of the Netherlands. Loads and production are compared for two distinct wind directions—a free wind situation from the dominating southwest and a full wake situation from northwest, where the observed turbine is operating in wake from five turbines in a row with 7D spacing. The measurements have a very high quality, allowing for detailed comparison of both fatigue and min–mean–max loads for blade root flap, tower yaw and tower bottom bending moments, respectively. Since the observed turbine is located deep inside a row of turbines, a new method on how to handle multiple wakes interaction is proposed. The agreement between measurements and simulations is excellent regarding power production in both free and wake sector, and a very good agreement is seen for the load comparisons too. This enables the conclusion that wake meandering, caused by large scale ambient turbulence, is indeed an important contribution to wake loading in wind farms. Copyright © 2012 John Wiley & Sons, Ltd.

KEYWORDS
wake effects; wind turbine; loads; power

Correspondence
Torben J. Larsen, Technical University of Denmark, Wind Energy Division, Building 118, PO Box 49, 4000 Roskilde, Denmark.
E-mail: tjul@dtu.dk

Received 6 January 2012; Revised 31 August 2012; Accepted 7 September 2012

1. INTRODUCTION

Wind conditions for wind turbines located inside wind farms are significantly different than outside farms. The main effects are that the average wind speed is decreased, and the turbulence inside the wind farm is increased. The result of this is a reduction in power production together with increased load levels. Several people have worked on the topic, and recent measurements of wake effects have previously been reported in Vølund,[1] Frandsen *et al.*,[2] Christiansen and Hasager,[3] Cleve *et al.*,[4] Barthelmie *et al.*[5] and Barthelmie and Jensen.[6] Many engineering models have been developed in the past. Regarding these models, the main focus has been to enable prediction of power production,[7,8] whereas only few models address the loading issues[9,10] and none of these models encompass both production and load aspects. The most well-known model for prediction of fatigue load levels is the one reported by Frandsen,[10] which is also the wake model included in the IEC61400-1 standard for load simulation of wind turbines. This model is basically a method to scale the intensity of the inflow turbulence according to the park configuration and the load component in question. This model is mainly based on full-scale load measurements observed from the Vindeby offshore wind farm in Denmark, where the turbines are located with a distance of approximately eight diameters. Remarkably, none of the previous mentioned models (with slight exception of Ainslie[8]) account for wake meandering even though this phenomenon was addressed by Baker and Stel[11] and Ainslie[8] in the 1980s. In order to enable simulation of the combined effect of both power reduction and load increase in a wind farm, a completely different type of model is needed. Different computational fluid dynamics (CFD) methods

have been demonstrated, where especially actuator line simulations seem promising.[12] Also large eddy simulations have provided new insight in the complexity of wind farm wakes.[13,14] Unfortunately, these methods are all very computationally demanding with simulation times of days or more on high performance computers and therefore not usable in typical load analysis for wind turbine design.

Another type of engineering model capable of predicting the loads on turbines inside wind farms is the dynamic wake meander (DWM) model, which is a more detailed model of the flow field behind the upstream turbine. This method uses the wind speed deficit of the upstream turbine together with a meandering process in order to simulate the incoming flow field of the downstream turbine and thereby enabling detailed analysis of both production and loading through aeroelastic computations. The meandering process causes an intermittent appearance of the flow field with periods of full, half or no wake situation—varying from time to time driven by the large-scale natural turbulence. This more correctly implemented physical process has previously been validated by load, inflow and wake measurements[15–18] and is further verified by this paper. It has also previously been seen that there are important differences in the turbine loading depending on the type of model chosen.[19,20]

1.1. The HAWC2 model

The HAWC2 code is an aeroelastic model intended for calculating wind turbine response in time domain.[21] The core of the code was mainly developed within the years 2003–2007 in the Aeroelastic Design Research Program at Risø, National Laboratory, Denmark, but is continuously being updated and improved.

The structural part of the code is based on a multi-body formulation as described in Shabana[22] using the floating frame of reference method. In this formulation, the wind turbine main structures are subdivided into a number of bodies, where each body is an assembly of Timoshenko beam elements. Each body includes its own coordinate system with the calculation of internal inertia loads when this coordinate system is moved in space; hence, large rotation and translation of the body motion are accounted for. Inside a body, the formulation is linear, assuming small deflections and rotations. This means that a blade modeled as a single body will not include the same nonlinear geometric effects related to large deflections of a blade divided into several bodies. The bodies, representing the mechanical parts of the turbine, are connected by kinematic constraints. The constraints are formulated as algebraic equations, which impose limitations of the bodies' motion. Examples of such constraints are a fixed connection from a structural node to a global point (e.g. tower bottom clamping), a fixed coupling of the relative motion (e.g. fixed pitch, yaw), a frictionless bearing and a bearing where the rotation angle is controlled by the user. It may be worth to notice that also for the last constraint where the rotation is specified externally, inertial forces related to this movement are accounted for in the response. External forces are placed on the structure in the deformed state, which is especially important for pitch loads and twist of the blades, and since large rotations are handled by a proper subdivision of bodies, the code is suited for calculations on very flexible turbines subjected to, e.g. large blade deflections. The structural model is general, but in its simplest form, a turbine is modeled using one body for the tower, one for the nacelle and one for each blade.

The aerodynamic part of the code is based on the blade element momentum (BEM) theory, but extended from the classic approach to handle dynamic inflow, dynamic stall, skew inflow, shear effects on the induction and effects from large deflections. One example is the effect of large flapwise blade deflections causing a change in the effective rotor diameter and that the blade forces are no longer perpendicular to the rotor plane. This reduces the thrust on the rotor and thereby changes the induced velocities and vice versa. The dynamic stall model[23] is a modified Beddoes–Leishmann[24] model that includes the effects of shed vorticity from the trailing edge (Theodorsen theory[25]), as well as the effects of stall separation lag caused by an instationary trailing edge separation point. These effects are important in relation not only mainly to flutter analysis, but also generally to calculate loads and stability of blades with very low torsion stiffness. The induced velocities are calculated on the basis of the local inflow velocities causing different inductions in the upper and lower parts of the rotor, as in the case of a large wind shear.[26] In order to illustrate the capability of this BEM implementation in the case of a wake situation with a turbine operating in a steady half wake from an upstream turbine, a phenomenological study was conducted in both HAWC2 and the CFD code EllipSys3D,[27] which generally is considered state-of-the-art within CFD simulation of flow around wind turbines. A very fine agreement was obtained, as seen in Figure 1.

The wind conditions are divided into deterministic and stochastic contributions. The deterministic wind is mean wind velocity, wind steps, ramps, special gust events and special shears, including the possibility for fully user-defined shears. The stochastic turbulent wind is generated using the Mann model,[28] which is a non-isotropic full three-dimensional correlated turbulence flow field model. Tower shadow effects are included using a potential flow method.

Control of the turbine is performed through one or more dynamic link libraries and is therefore not part of the HAWC2 core. The reason for this is that each turbine is equipped with its own individual controller, which is normally kept confidential by the manufacturer.

The calculation time, which is obtained using a Newmark-beta solution scheme together with Newton–Raphson iterations within each time step, is approximately a factor of 1–2 slower than real time on a 3 GHz CPU.

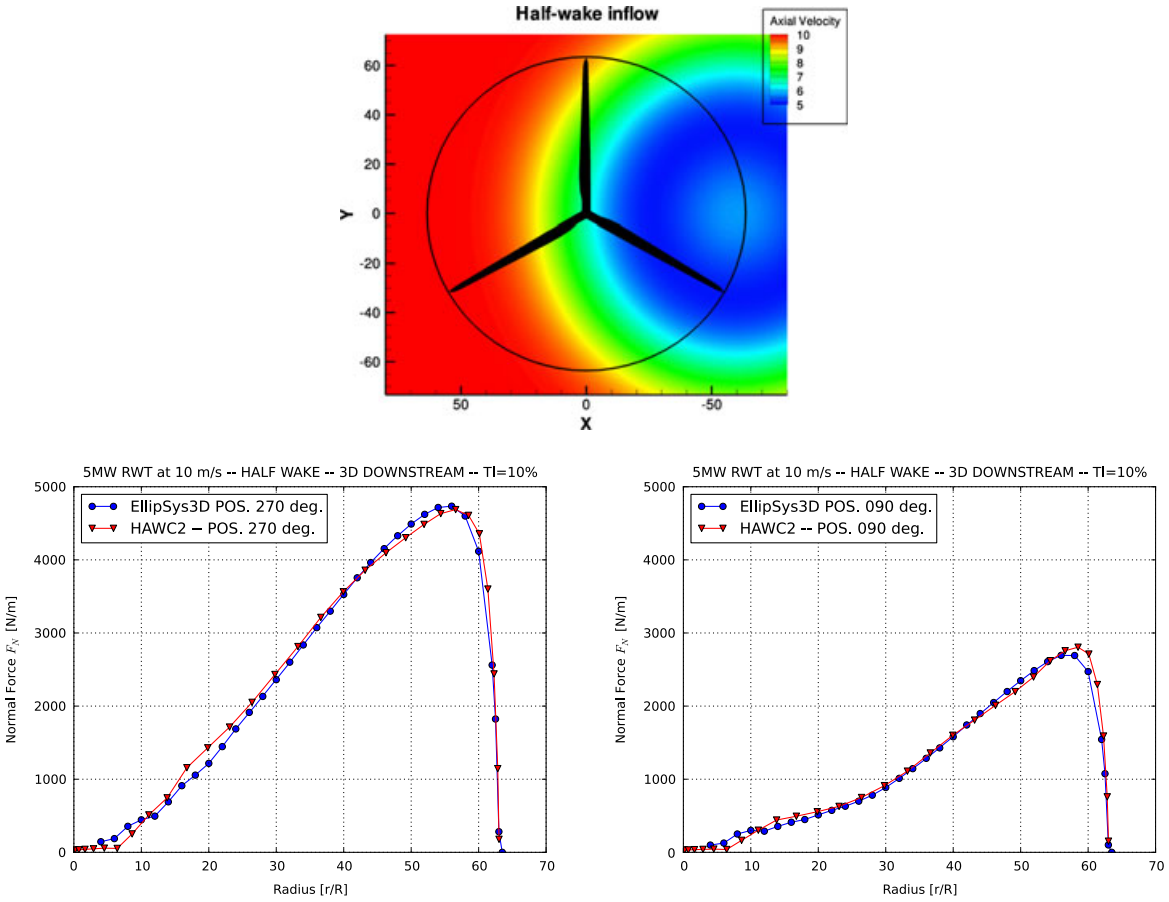

Figure 1. Comparison between EllipSys and HAWC2 results of axial forces on a blade in a constant half wake situation. Blade 1 is 270° to the left and 90° to the right.

2. THE DWM MODEL AND COMPARISONS WITH MEASUREMENTS FOR THE EGMOND AAN ZEE WIND FARM

2.1. The DWM model

The DWM model complex is based on the combination of three corner stones: (1) modeling of quasi-steady wake deficits,[16] (2) a stochastic model of the down wind wake meandering and (3) added or self-generated wake turbulence (Figure 2).

The quasi-steady wake deficit is the wake deficit formulated in the moving (i.e. meandering) frame of reference and includes the wake expansion as a function of downstream transportation time caused partly by turbulence diffusion and partly by recovery of the rotor pressure field. The modeling of this deficit is based on a thin shear layer approximation of the Navier–Stokes equations in their rotational symmetric form combined with an eddy viscosity closure. The initial condition is constituted by the induced wind field in the rotor plane determined from a BEM approach. In the present formulation, the aerodynamic module of HAWC2 is used for this purpose. Further details on the implementation can be found in Madsen *et al.*[16]

The wake meandering part is based on a fundamental presumption stating that the transport of wakes in the atmospheric boundary layer can be modeled by considering the wakes to act as passive tracers driven by the large-scale turbulence structures in lateral and vertical directions.[29] Modeling of the meandering process consequently includes considerations of a suitable description of the 'carrier' stochastic transport media as well as a suitable definition of the cutoff frequency defining large-scale turbulence structures in this context. For the stochastic modeling of wake meandering, we imagine the wake as being constituted by a cascade of wake deficits, each 'emitted' at consecutive time instants in agreement with the passive tracer analogy.[29,30] We then subsequently describe the propagation of each of the 'emitted' wake deficits,

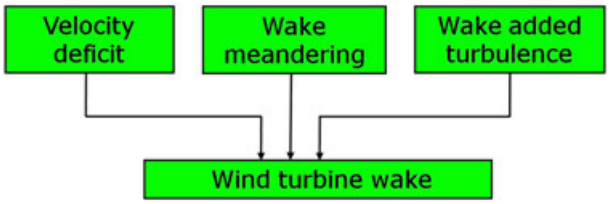

Figure 2. Overview of the three fundamental parts of the DWM model.

and the collective description of these thus constitutes the wake meandering model. Adopting Taylor's hypothesis,[31] the downstream advection of these is assumed to be controlled by the mean wind speed of the ambient wind field. With this formulation, the wake momentum in the direction of the mean flow is invariant with respect to downstream displacement. This is a considerable simplification allowing for a straight forward decoupling of the wake along the wind deficit profile (and its expansion) and the wake transportation process. As for the dynamics in the lateral and vertical directions, each considered wake cascade element is displaced according to the large-scale lateral and vertical turbulence velocities at the position of the particular wake cascade element at each time instant. The choice of a suitable stochastic turbulence field, that in turn defines the stochastic wake transport process, is not mandatory, but may be guided by the characteristics of the atmospheric turbulence at the site of relevance. These characteristics encompass in principle not only turbulence standard parameters such as turbulence intensity, turbulence length scale and coherence properties, but also features such as degree of isotropy, homogeneity of the turbulence, Gaussianity of the turbulence, etc. The meandering mechanism in the DWM model was initially verified for small turbine distances by pitot tube measurements on a Neg Micon NM80 turbine[19] and later verified by correlating DWM predictions with direct full-scale measurements of the instantaneous wake position obtained from light detection and ranging (LiDAR) recordings.[17]

In this paper, the turbulence box for the meandering process is generated using a transverse and vertical resolution of one diameter, whereas the distance between the turbulence grid points in the time axis is 0.07 s. Further on, a low pass filter on the transverse wake position is applied in order to exclude contributions from turbulence eddies with a characteristic scale smaller than two rotor diameters.[29] The physical reasoning behind this is that atmospheric vortex structures smaller than $2D$ tend to change the deficit mixing process rather than contribute to distinct meandering. The filter cutoff frequency is defined by the distance $2D$ and the mean free wind speed U_0

$$f_0 = \frac{U_0}{2D} \tag{1}$$

The added wake turbulence includes contributions from conventional mechanically generated turbulence, caused by the wake shear, as well as from the blade-bound vorticity, consisting mainly of tip and root vortices. In analogy with the description of the wake deficit, the added wake turbulence is formulated in the meandering frame of reference. In the present context, a simple scaling in the radial direction of a (small-scale) turbulence field originating from the Mann spectral tensor is adopted. The suggested scaling factor depends on the magnitude of the quasi-steady wake deficit as well as of the wake-deficit radial gradient. Further details can be found in Madsen *et al.*[16]

The required input to the DWM model in its present implementation is wind farm topology information and conventional aerodynamic wind turbine blade data supplemented by ambient wind field information such as mean wind speed and turbulence intensity.

2.2. How to handle multiple wakes in the DWM model

An important problem to address when modeling wake effects deep inside a wind farm is how to handle wakes from multiple turbines. This is not straightforward, since the deficit from one turbine interferes with the next turbine and is further complicated by the turbulent mixing process recovering energy downstream. In order to investigate the interaction of wakes, five turbines in a row with $8D$ spacing were studied for operating conditions of 8 m s^{-1} and a turbulence intensity of 2%, see Figure 3. The motivation for using a turbulence intensity of 2% is to reasonably neglect the meandering influence, since the effect of meandering is addressed separately using the meandering approach described in Section 2.1. The inflow wind speed to each individual turbine was reduced with two-third at the rotor area—corresponding to the far field value for an ideal turbine with induction of one-third—and further expanded radially by 30% to account for wake pressure expansion. The quasi-steady wake deficit at $8D$ downstream location behind each turbine was found using the axis-symmetric flow solver described in Madsen *et al.*[16] based on the eddy viscosity concept. This deficit was inserted successively in the same loop described earlier (wind speed reduction to one-third, pressure expansion, flow solver) for the following downstream turbines, until the final deficit at the $40D$ downstream location was found. This is shown in Figure 3 together with deficits

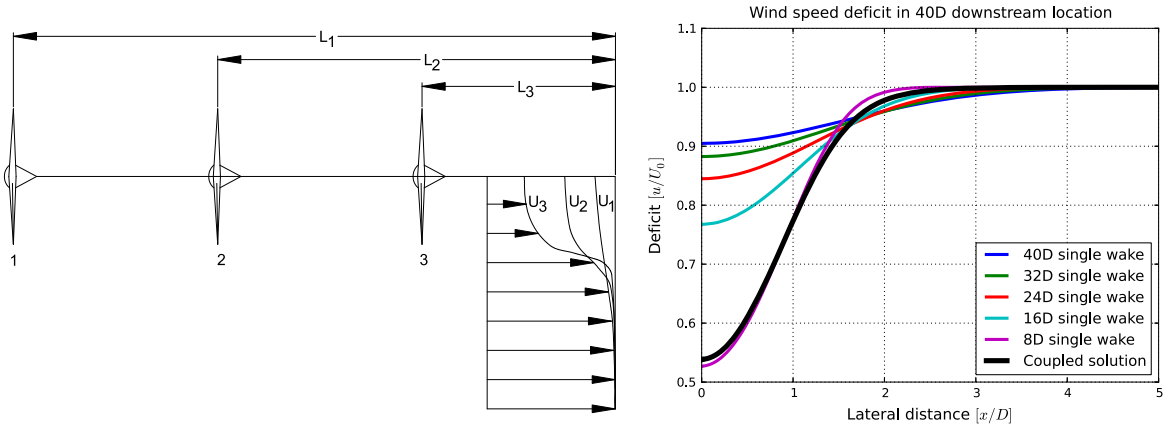

Figure 3. Illustration of the principles behind multiple wake deficits without effects of meandering. (Left) Turbine configuration showing the first three turbines in a row of five turbines and their individual deficits. (Right) Final individual deficits of the five upstream turbines separated with eight diameters as calculated with the axis-symmetric eddy viscosity model compared with a coupled solution including all turbines.

at $8D$, $16D$, $24D$, $32D$ and $40D$ downstream distances for a turbine operating at 8 m s^{-1}. When observing this figure, it can be seen that the final deficit has huge similarities with the $8D$ deficit for small radial locations and larger similarities with the $40D$ deficit for large radial positions. This motivates an approach for interacting wakes where the strongest deficit at a given downstream location can be used when observing wakes from multiple turbines. This forms the basis for the selection approach formulated in (2) at a given position, here simply noted with r for radius.

$$u_{\mathrm{def,final}}(r) = \min(u_{\mathrm{def},1}(r), u_{\mathrm{def},2}(r), \ldots, u_{\mathrm{def},N}(r)) \tag{2}$$

where i is turbine number running 1 to N turbines in the park.

The frequency scales involved in the wake meandering process are very low and therefore assumed to be independent of flow disturbances from other turbines, since these mainly affects high frequencies, hence smaller vortex scales. The low frequency part of the turbulence corresponding to large vortex scales is to some extent similar for neighboring turbines causing the wake pattern to meander in correlated traces. When turbines are positioned after each other in a row, the downstream turbine only experiences full wake conditions once in a while as illustrated in Figure 4, which further justifies the assumption of treating wake deficits individually as described in (2).

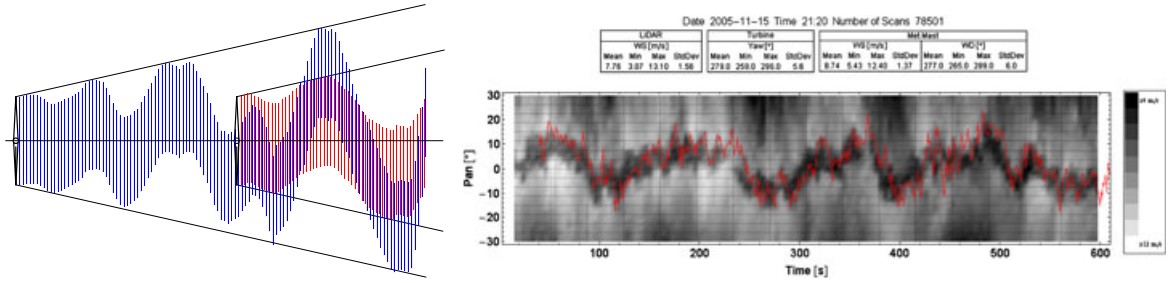

Figure 4. (Left) Illustration of wake pattern according to the DWM theory. The downstream turbine is only once in a while subjected to full wake loading even though the lateral movements to some degree are coherent. (Right) Full-scale LiDAR observations of wake meandering in a downstream flow cross-section, three rotor diameters downstream of the wake-generating rotor. The measured wake meandering as a function of time is the black track (i.e. low wind speeds). The red line is the DWM prediction of the wake deficit position based on observed spatially averaged instantaneous rotor inflow direction fluctuations. The measurement is from the campaign reported in Bingöl *et al.*[17]

2.3. Recalibration of the coupling between the eddy viscosity and ambient turbulence in the DWM model

A detailed description of the modeling of the quasi-steady wake deficit in the DWM model can be found in Madsen *et al.*,[16] where also different verification cases against the CFD actuator line (AL) model results are presented. Further work on validation of the model was carried out within the European Research Project TOPFARM,[32] where full-scale measurements of power reduction in different wind farms as a function of turbulence intensity became available. In Figure 5, the power reduction for the second turbine in a row relative to the first turbine is shown as function of turbulence intensity for the wind direction aligned with the row. The data are extracted from three different wind farms with different turbine spacings. A strong influence of the turbulence intensity on the power reduction is seen. The reason for this dependence on turbulence level is explained not only by an increased turbulence mixing but also by an increased amount of meandering. The parameters in the DWM model relating the ambient turbulent intensity to the eddy viscosity were now recalibrated using this data set. The calibrated DWM model results are also shown in Figure 5, and the results compare well with the measurements. In order to correlate the experimental data set with model data, it turned out to be very important to perform the load simulations covering the full range of measured wind speeds (6–12 m s^{-1}) as well as the full direction sector ($\pm 5^{\circ}$) which were the conditions for the experimental data. The reason for this is the very nonlinear behavior of power performance with turbine load level and free, half and full wake situations.

In the first version of the model, described in Madsen *et al.*,[16] where the coupling of the eddy viscosity to ambient turbulence intensity was based only on a comparison with AL model results, the non-dimensional eddy viscosity υ_T^* was coupled to the ambient turbulence intensity I_{amb} by the following relation:

$$\upsilon_T^* = F_2 k_2 \left(\frac{b}{R}\right)\left(1 - \frac{U_c}{U_H}\right) + F_1 k_{amb} I_{amb} \tag{3}$$

where F_1 is a filter function modeling the delay in entrance of ambient turbulence into the wake, F_2 is a second filter function defined in Madsen *et al.*,[16] $\frac{b}{R}$ is the instantaneous wake half width normalized by the rotor radius, U_c is the minimum wake wind speed, U_H is ambient wind speed at hub height wind speed, and k_{amb} is an empirical constant determined to be 0.07. Further details can be found in Madsen *et al.*[16]

Using this calibration, deviations from the full-scale data shown in Figure 5 were found for low turbulence intensities in combination with moderate to high spacings, where the model gave too low recovery of the velocity deficit. To improve the performance, a nonlinear coupling function F_{amb} of the eddy viscosity to ambient turbulence intensity was introduced in combination with a modified filter function F_1 in order to delay the entrainment of the ambient turbulence, because a

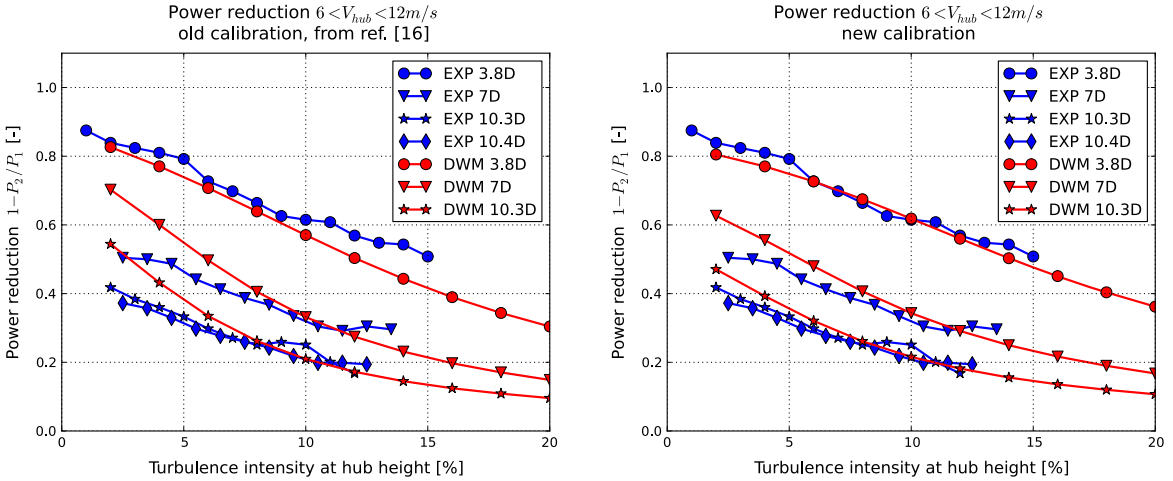

Figure 5. Power reduction as function of turbulence intensity measured for three different spacings and compared with DWM results. The experiments are carried out for three different wind farms; 3.8D = Wieringermeer (NL),[33] 7D + 10.4D = Horns rev (DK)[34] and 10.3D = Nysted (DK).[6] (Left) Comparison between measurements and DWM model from the version described in Madsen *et al.*[16] (Right) Comparison with DWM with the modification from this paper. A small influence of the new calibration is seen and it leads to slightly improved correlation with measurements at low ambient turbulence. P_1 refers to the upstream turbine and P_2 to the downstream.

DOI: 10.1002/we

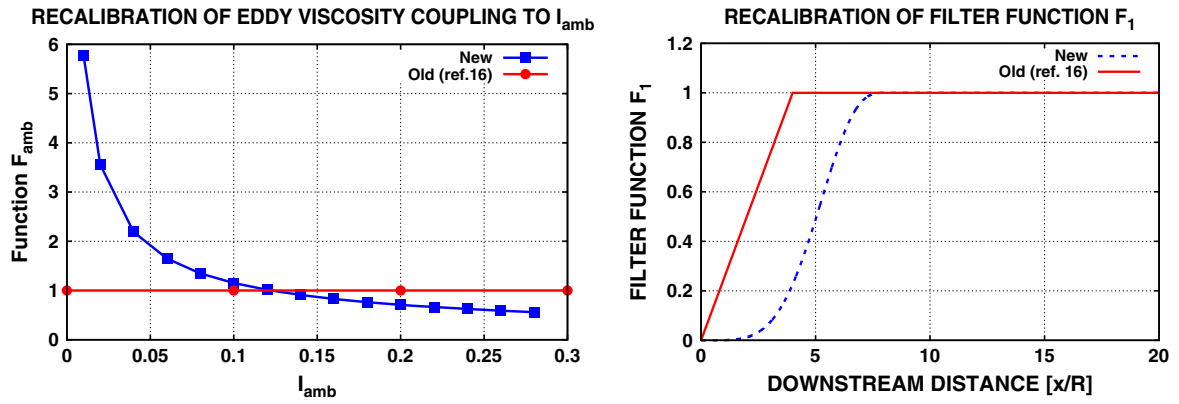

Figure 6. (Left) The new nonlinear coupling function F_{amb} based on a calibration with full-scale measurements of power reduction as function of ambient turbulence. (Right) The modified filter function F_1 based on a calibration with full scale measurements of power reduction as function of ambient turbulence.

relative good correlation already was present for the low spacing and low turbulence intensity cases:

$$\upsilon_{\text{T}}^{*} = F_2 k_2 \left(\frac{b}{R}\right)\left(1 - \frac{U_{\text{c}}}{U_{\text{H}}}\right) + F_1 F_{\text{amb}} k_{\text{amb}} I_{\text{amb}} \tag{4}$$

The new nonlinear coupling of F_{amb} to I_{amb} is shown in Figure 6 (left) and the modified filter function in Figure 6 (right) and the simulations have been run with k_{amb} equal to 0.10.

2.4. Measurements at the Egmond aan Zee wind farm

The Egmond aan Zee wind farm is located outside the coast of the Netherlands and consists of 36 Vestas V90 3.0 MW wind turbines installed on monopile foundations. The layout of the wind farm consisting of four rows of turbines can be seen in Figure 7. The distances between the rows are $10.5D$, whereas the turbine spacings within the rows are $7.3D$. The wind turbine WT7 is located on 17 m water depth and the pile diameter is 4.6 m with a thickness of 50 mm.[35] The transition piece is also modeled using these dimensions. A structural damping of 2% in terms of logarithmic decrement is used for all turbine vibration modes except for the tower mode, where 1% is applied.

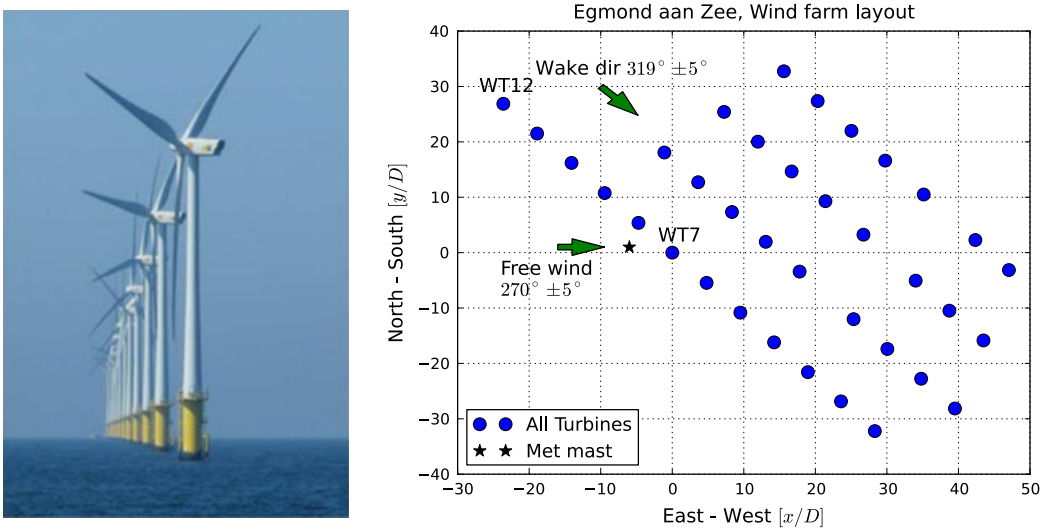

Figure 7. (Left) Photo of the V90 turbines at Egmond aan Zee. (Right) Position of turbines in farm relative to WT7. Distance is non-dimensionalized with rotor diameter.

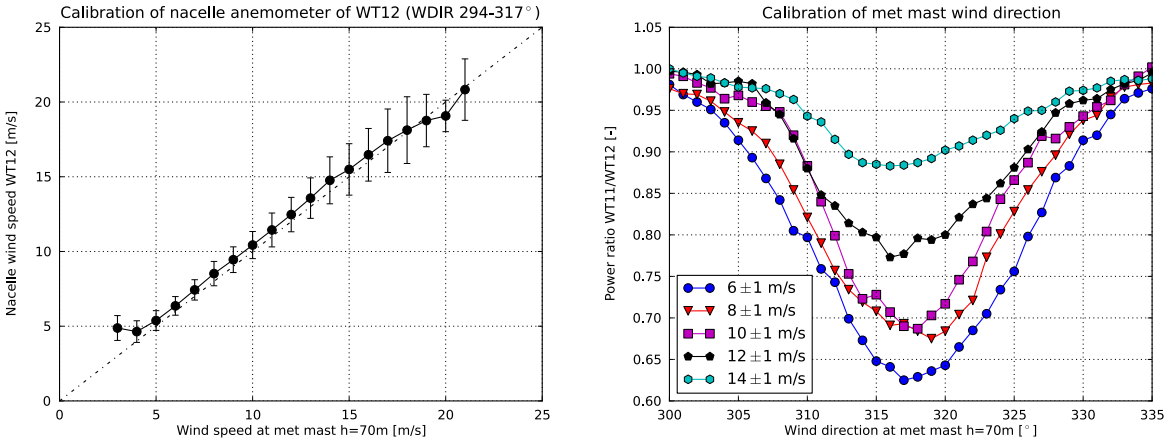

Figure 8. (Left) Correlation between wind speed measured with nacelle-mounted anemometer on WT12 and met mast at hub height. (Right) Power ratio between WT11 and WT12 for wind speed bin intervals; $W_{hub} = 6$, 8, 10, 12 and 14 ± 1 m s^{-1} as the function of reference wind direction from the met mast.

One meteorological mast (met mast) is located at the site southwest of WT8, see Figure 7, which is the dominant wind direction at the site. At the met mast, the wind speed and direction are measured at three heights: 116, 70 and 21 m, where 70 m corresponds to the turbine hub height. The met mast wind direction sensors are calibrated on the basis of power measurements of WT21, where the lowest power production was expected at 196° because of the layout of the wind farm. The calibration of the met mast data is explained in detail in Johansen,[36] where an uncertainty level of 1.4° on the final measured wind direction is concluded. The two wind turbines WT7 and WT8, located in the southwest row, are equipped with structural measurement and WT7 is used for load comparisons in this paper since the measurements for WT8 were out of operation for a longer period. The structural measurements are based on strain gauge recordings at the blade root bending in edge and flapwise direction at radius 3.6 m. Tower moments are measured at 17.9 m height above mean sea level (MSL). The yaw moment is measured at 63.4 m height above MSL. In addition to the high resolution structural measurements, a supervisory control and data acquisition (SCADA) system records 10 min statistics for all the installed turbines. The SCADA data set includes electrical power, rotor revolutions per minute, pitch angle, generator revolutions per minute, yaw orientation and nacelle wind speed.

In general, the measured loads are of high quality. No significant drift in gauges is observed. However, because the location of the met mast is very close to the wind turbines, wake effects are preventing a correct measurement of the free wind speed except for the free sector with wind from south to west. In order to determine the free wind when the wind is from 319°, the nacelle cup anemometer on WT12 was used after first being calibrated against the met mast for free wind directions, Figure 8. This clearly demonstrates that the nacelle wind speed at WT12 can be used to measure the free wind, which enables a measurement of wind speed for 319° inflow, where the met mast was affected by wakes. In order to obtain a reliable measurement of the wind direction, similar problems with the met mast were faced. The wind vane of the met mast was therefore calibrated using a similar procedure as for the calibration in the free sector, now based on power ratios between WT11 and WT12, shown in Figure 8. The wake direction is seen to be 319° using this sensor at 8 m s^{-1} only, where small corrections are needed for different wind speeds. The conclusion is that the met mast can be used for the free wind direction, whereas the calibrated nacelle wind speed from WT12 and the calibrated wind direction from the met mast are used for the wake sector.

2.5. Implementation and tuning of the collective pitch controller for the V90 turbine

The V90 turbine has been modeled on the basis of structural and aerodynamic data provided by Vestas. The controller was, however, not a part of this delivery, and a general pitch, variable speed controller was tuned for the turbine. The controller type and tuning procedure have previously been described in Larsen and Hanson,[37] however, a few improvements were performed to ensure a proper performance in the low wind speed region, where the variable speed is active. This also includes improvements to the control mode transition between the modes' variable speed, optimal power and full power production. The diagram of the controller content is illustrated in Figure 9. The fundamental part of the controller is the measurement of the rotational speed of the rotor. This rotor speed is low pass filtered (1) to avoid high frequent excitation into the controller. It is especially important to have a cutoff frequency lower than the drive train frequency dominated by the free inertia of the rotor and generator through a gearbox and a flexible shaft connection. This mode is normally referred

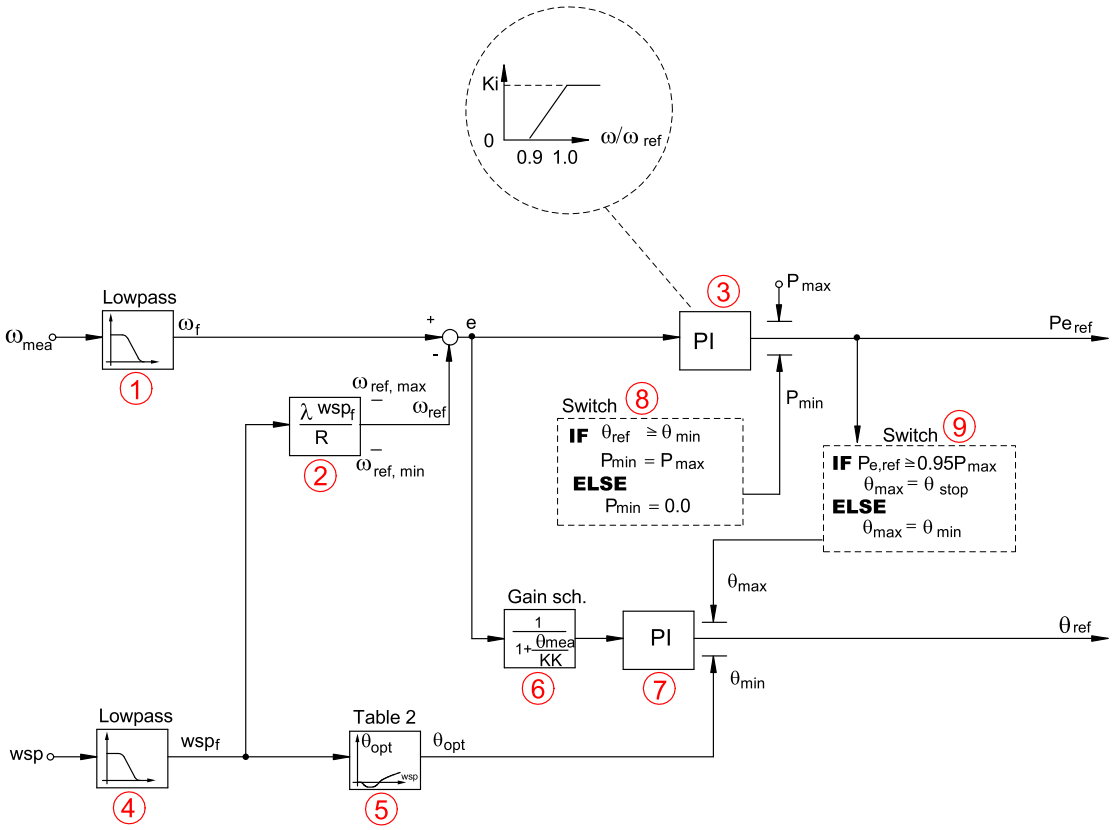

Figure 9. Control diagram of the developed collective pitch controller. The control of pitch angle and generator power is based on measurement of rotor and wind speeds only. The wind speed measurement is only of importance below rated rotor speed.

to as the free–free drive train mode. The difference between the filtered rotor speed and a reference nominal rotor speed is input to a proportional–integral (PI) controller of the generator power (3). This PI controller increases/decreases the generator power, when the rotor speed is higher/lower than nominal within limitations. The limitations are the rated power as the upper limit, whereas the lower limit depends on a logical switch (8) based on the output for the reference pitch angle. This switch controls the shift between limited rotor speed and full power production. In full power production, the minimum limitation equals the maximum limitation causing the reference power output to be constant. A second order low pass filter is applied on this minimum limitation value to ensure a smooth transition between control modes (not shown). A new approach for controlling the variable rotor speed in low wind speed is the removal of integral gain in the PI controller, when rotor speeds are below 90% of rated speed (3). This actually transforms the behavior of generator into an asynchronous generator characteristic with controllable reference speed, since the generator torque only depends on generator velocity and reference speed. This causes a smooth and highly damped response of the system for low wind speeds. The reference rotor speed is set based on an optimal tip speed ratio λ and measurement of the nacelle wind speed filtered through a low pass filter (4). Minimum and maximum rotor speeds are ensured in (2). The rotor speed variation is also the essential input value for the PI control of the reference pitch angle (7). This PI controller is gain scheduled through the compensation term in (6), fully described in Hansen *et al.*[38] This gain scheduling of the proportional and integral gain in (7) is important to counteract the varying $\frac{\partial P}{\partial \theta}$ characteristic of the rotor for different pitch angles θ. The parameter KK is defined as the pitch angle where $\frac{\partial P}{\partial \theta}$ is twice as high as at the rated wind speed with a pitch angle of 0°. The minimum limitation value of (7) is a simple way of handling optimal pitch variation at low wind speeds through a table lookup in (2), which provides the optimal pitch angle as function of the low pass filtered nacelle wind speed (4). The maximum pitch angle limitation in (7) is very importantly related to the control transition to full power operation. When the generator power is above 95% of rated power, the limit changes from the minimum limit value (where the PI control is then bypassed) to the stop pitch angle of 90°, which enables active pitch control. The changed value of $\theta_{\max}$ is low pass filtered to ensure a smooth transition (not shown).

As a validation of the controller, the statistics of a few key sensors have been shown in Figure 10. In general, a very good agreement is seen for pitch, rotor speed and power production. Minor differences are, however, also visible. Regarding the

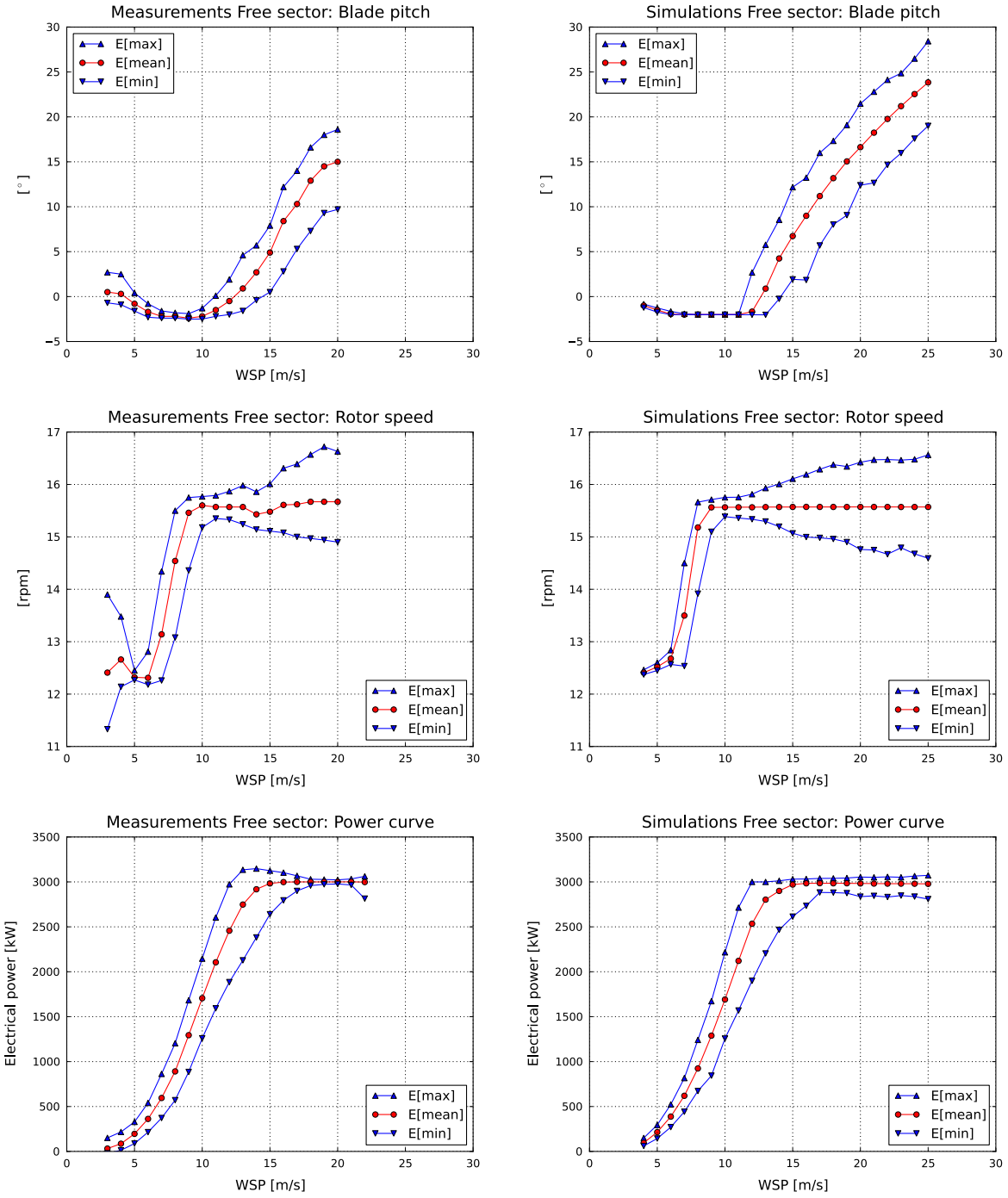

Figure 10. Comparison in the free sector between key sensors for the control system behavior. (Left) Measurements and (right) simulations.

pitch angle, it can be seen that a higher variation is seen for small wind speeds, which may be caused by a higher variation in turbulence intensity at these low wind speeds and a more active control strategy. Since this only affects wind speeds at 3–4 m s^{-1}, the importance is considered minor. At above rated wind speeds, the average pitch angle is offset with 2°. This is caused by either an offset error in the measurement or a difference in the aerodynamic load, since the pitch angle is automatically adjusted by the controller to keep the rotor speed at rated level. Especially the airfoil data at the tip of blade

should perhaps have had a larger negative $C_{l,\max}$ at negative angle of attack, but it has not been possible to clarify this. For the rotor speed variation, it is seen that the controller in the simulation has a slightly higher tip speed ratio causing the rated speed to be obtained at lower wind speeds than in the measurements. A larger variation in rotor speed is also

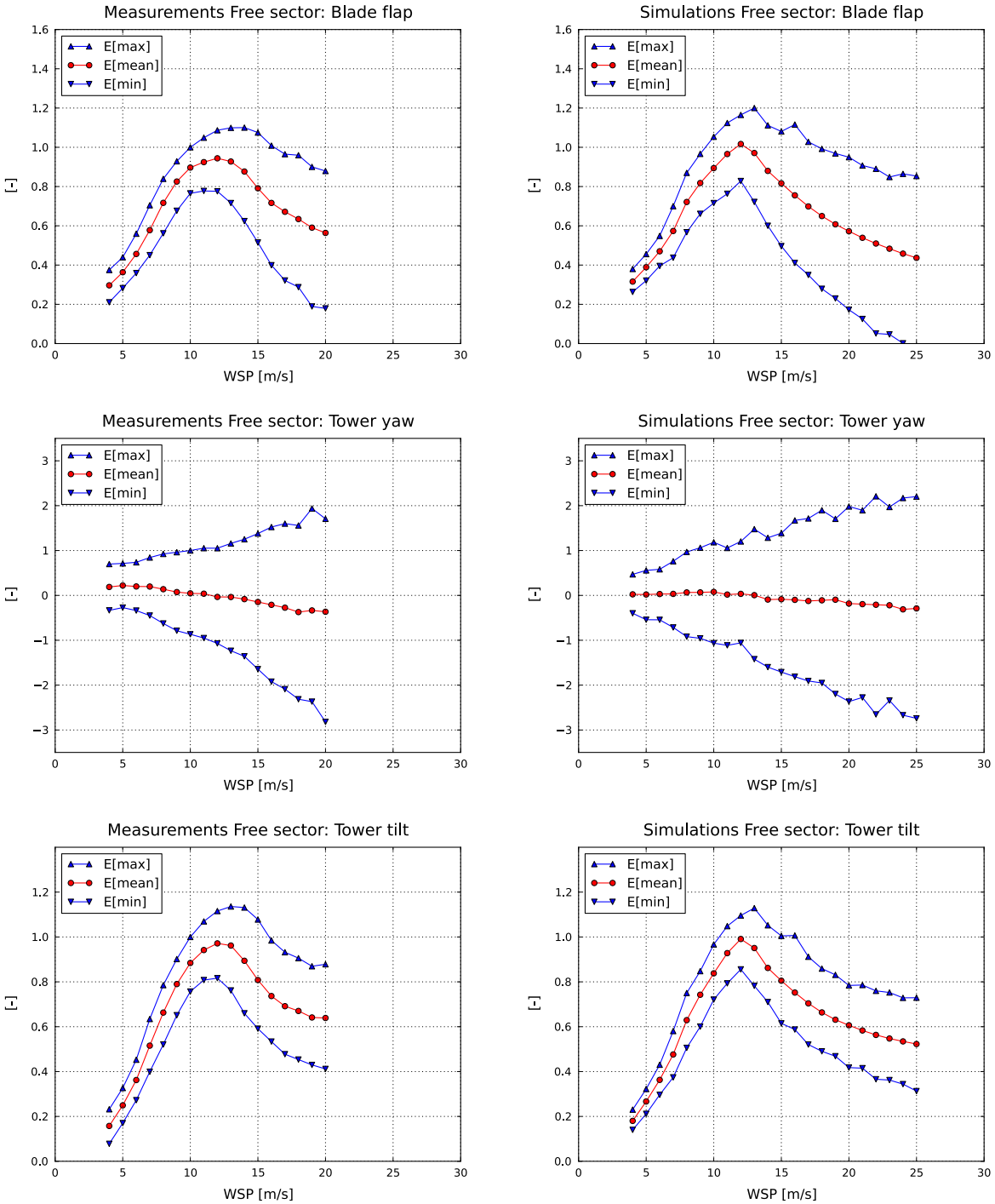

Figure 11. Comparison of statistics for selected moment signals in the free sector. (Left) Measurements and (right) simulations. The loads have been normalized with the average max load in the measurement at 10 m s^{-1}. An agreement within 5–10% is seen, which is considered very good. The E[] denotes a mean value operator.

seen at 3–4 m s^{-1}, which, as for the pitch angle, is considered of minor importance. The power curves are in very fine agreement for the mean level, but it can be seen that a slightly different strategy just below rated wind speed is applied in

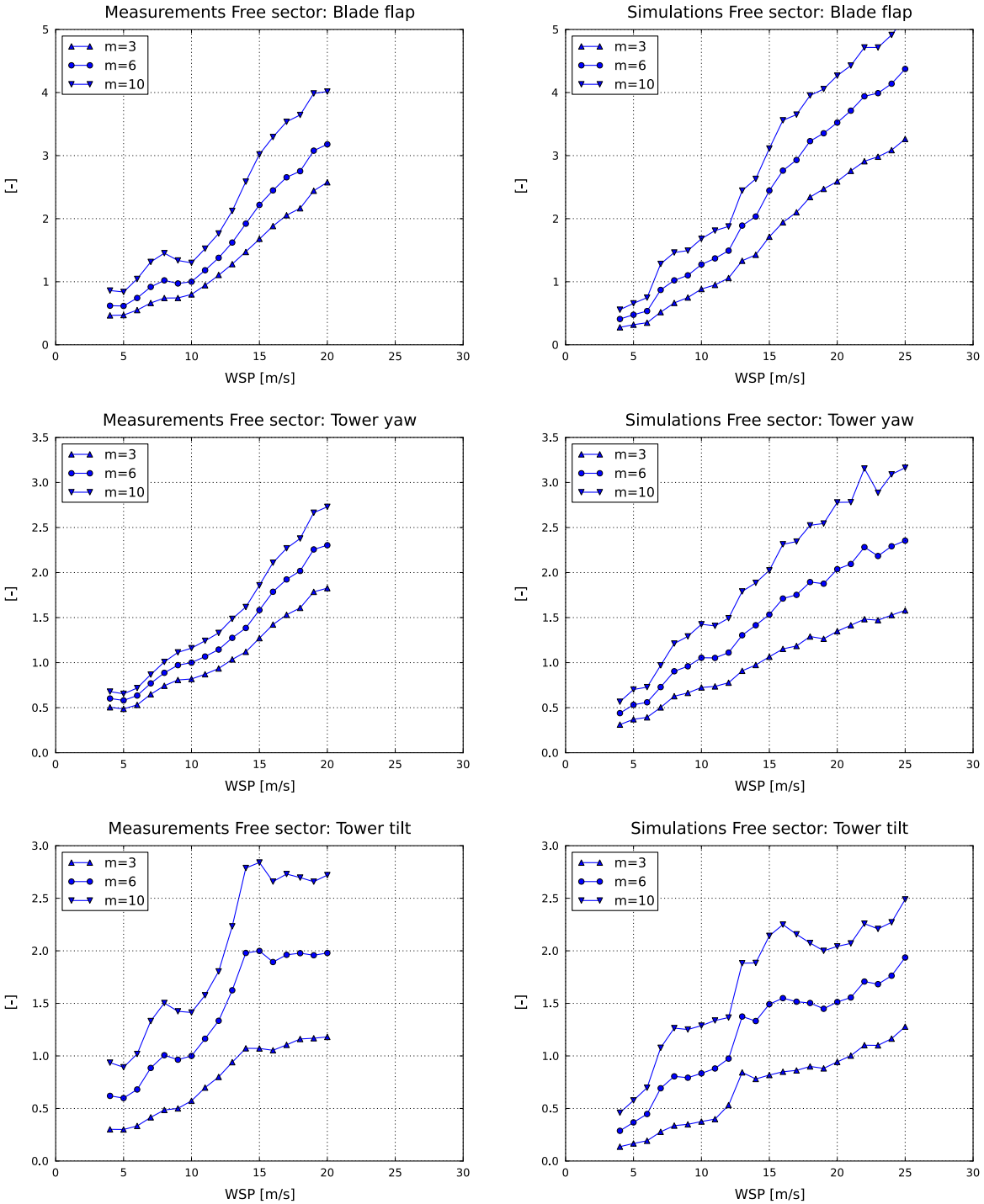

Figure 12. Comparison of 1 Hz equivalent fatigue loads for selected moment signals in the free sector. (Left) Measurements and (right) simulations. The loads have been normalized with the equivalent measured load for Wöhler material exponents $m = 6$ at 10 m s^{-1}. A good agreement is seen for the flap and yaw loads, where larger differences are seen for the tower bending moment.

the measurement. A kind of power 'boost' is apparently applied to increase the power output above rated, when the wind speed increases above rated for short periods due to turbulence variations, which is not present in the simulations.

2.6. Comparison between HAWC2 simulations and measurements for a turbine in the free sector

Simulations have been compared with full-scale measurements in term of statistics and 1 Hz equivalent fatigue loads. These are plotted in Figures 11 and 12 in a non-dimensional form, normalized with the measured loads at 10 m s^{-1}. Even though the V90 is placed at 15 m water depth, the wave loads have not been modeled, since the information about these conditions is not present to the authors' knowledge. The lack of wave loading might explain some of the deviance in especially tower loads seen in Figure 12. However, since the sensor location is 17.9 m above water level, the wave load impact is considered of very limited importance, and the full explanation for the deviances thus not found.

In Figure 11, a comparison of the statistics has been shown. In the measurement, each data point represents the mean value of a number of 10 min measurements. The number of 10 min time series depends on the wind speed, but generally there are 100–200 time series for wind speeds between 5 and 15 m s^{-1}. For higher wind speeds, the number of measurement decreases 'linearly' with wind speed to three cases at 20 m s^{-1}. Each point in the simulations represents nine half-hour simulations (three stochastic independent realizations obtained by using three different seed values for the turbulence generator combined with $+10°$, $0°$, $-10°$ yaw error). The reason for using half-hour simulation is to improve the statistical significance as well as to include more low-frequency turbulence than possible for a normal 10 min simulation. Every wind speed is simulated with a turbulence intensity matching the average measured turbulence intensity, which is shown in Table I.

Regarding the statistics for blade loads, longitudinal tower loads as well as tower yaw loads, there is a very good agreement between simulations and measurements. As for the differences, it can be seen that the simulated mean blade flap loads are slightly higher than in the measurements. All the max–min loads are in good agreement.

In Figure 12, the 1 Hz equivalent fatigue loads are shown for blade flap, yaw and tower bending for three different Wöhler material exponents $m = 3$, 6 and 10 representing steel, high quality steel and composite materials, respectively. The rainflow algorithm used to measure the fatigue load contribution is found in Matsuishi and Endo[39] and Dowling.[40] The reason for showing the results for the different m-values is to enable interpretation of the differences related to big and small load cycles, since large m-values are sensitive to the few large load cycles, whereas small m-values are sensitive to many small cycles. In general, the agreement between measured and simulated fatigue loads is good, however, above rated wind speed differences are seen. Measured and simulated blade flap and tower yaw loads are in good agreement regarding both statistics and fatigue loads. The deviances for the tower load comparisons are considerably larger, where measured fatigue loads are 25% larger than simulated. The max–mean–min loads are however in good agreement for the tower loads. The explanation for the observed difference in tower loads is not yet fully understood, and the tower load comparisons should therefore be interpreted with caution.

2.7. Comparison between HAWC2/DWM simulations and measurements for a turbine in the wake sector

Measurement data extracted from the wake sector of $319° \pm 5°$ have been compared with simulations. As previously described, a problematic issue is that the met mast data cannot be used for this direction sector, since the wake from the turbines WT8–WT12 is influencing the wind measurements. This problem was solved using the cup anemometer and turbine orientation at turbine WT12 calibrated against the met mast in the free sector. Since the wind direction corresponding to the wake sector is rarer than the free sector, each measurement point represents an average value for a narrow $10°$ sector ($319° \pm 5°$). The corresponding free sector represents a $90°$ sector ($225° \pm 45°$). In order to match the measurement conditions, simulations have been conducted using half-hour simulations with three different seed values (as for the free wind simulations), but further simulated at wind directions $-5°$, $-2.5°$, $0°$, $2.5°$ and $5°$ representing the real wind farm wind directions $-314°$, $-316.5°$, $319°$, $321.5°$ and $324°$.

Table I. Relation between mean turbulence intensity, shear exponent and wind speed, from Johansen.[36]

Wind speed $[m\ s^{-1}]$	4	5	6	7	8	9	10	11	12	13	14	15	16	17	18	19	20
Turbulence intensity [%]	6.8	6.3	5.9	5.8	5.6	5.6	5.6	5.6	5.9	6.0	6.1	6.2	6.3	6.3	6.4	6.2	6.2
Shear $\alpha * 100$	9	9	10	11	11	11	11	13	13	14	14	15	17	18	19	20	20

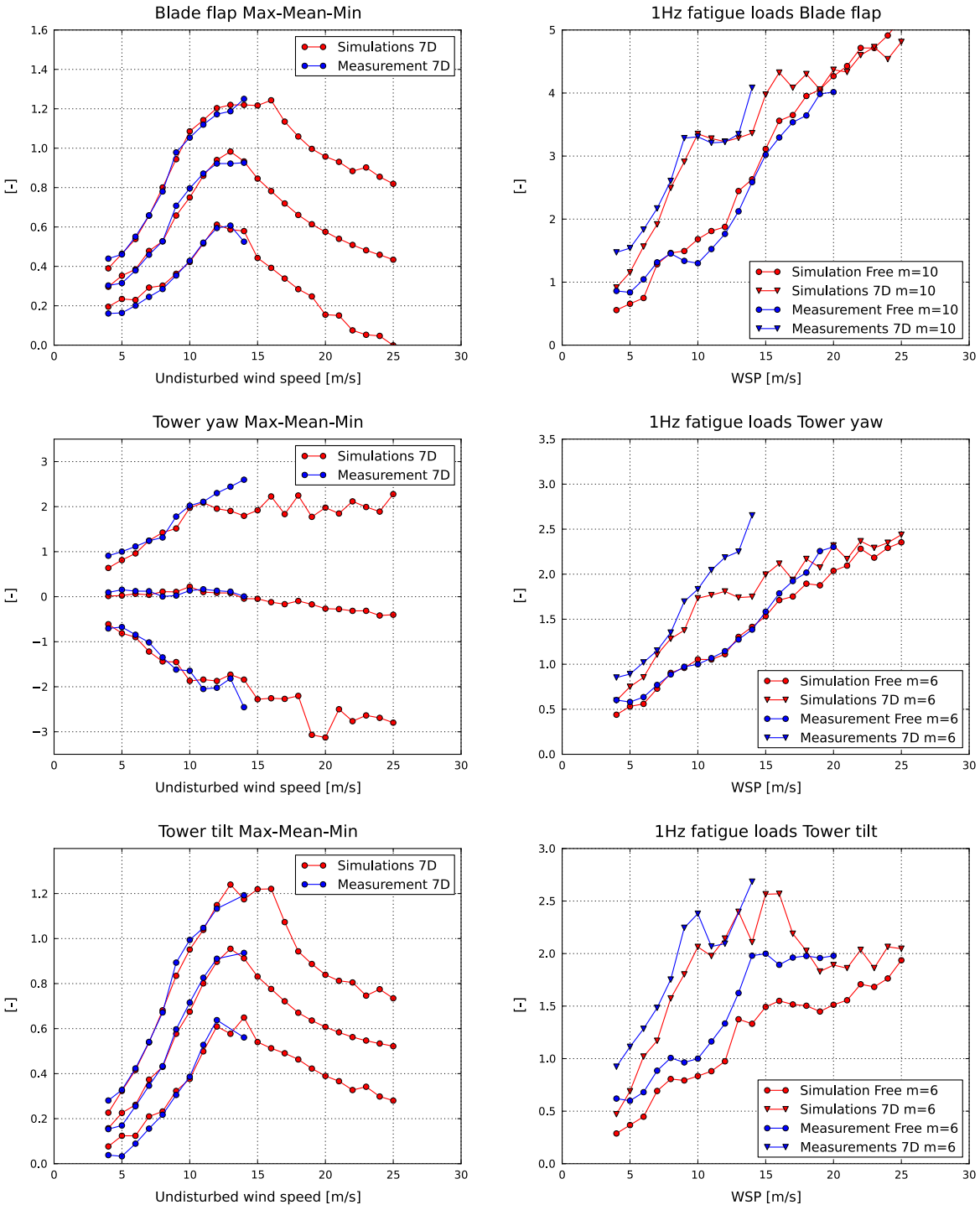

Figure 13. Comparison of simulation and measurements for selected moment signals in the free sector and 7*D* wake. (Left) Statistics of 7*D* sector showing maximum, mean and minimum values as in Figure 11 and (right) 1 Hz equivalent fatigue loads for a selected *m* value at both free and 7*D* wake situation. The statistical loads have been normalized with the average max load in the measurement at 10m/s for the free sector. The fatigue loads have been normalized with the equivalent measured load for Wöhler material exponent m=6 at 10m/s for the free sector.

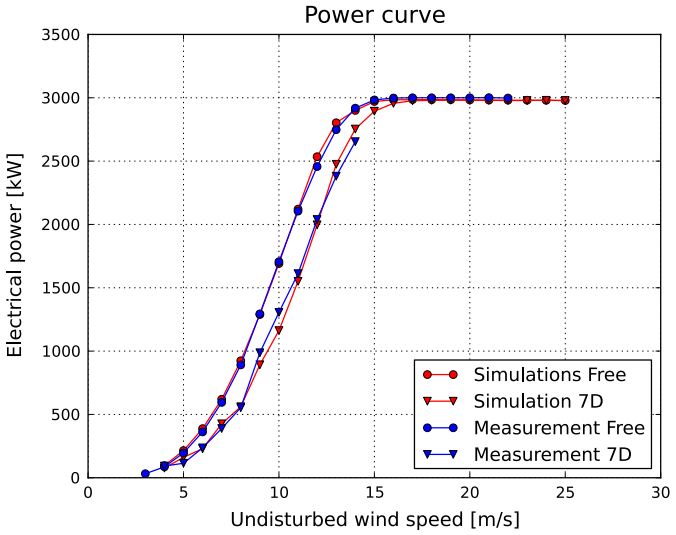

Figure 14. Power curve comparison between measurements and simulations is shown for the free and 7*D* wake sector with the turbine in wake of five upstream turbines. The undisturbed mean wind speed has been used as independent variable in both cases. A very fine agreement is seen.

In Figure 13, the statistics and fatigue load results are shown for the wake sector. For the fatigue loads, the results for the free sector are also shown. This enables not only a comparison between measurements and simulations, but also a comparison of free versus wake sector results. Only fatigue results for the most representative material parameter of the sensor are shown. In the measurement, each data point represents the mean value of a number of 10 min measurements. There are 11 time series for wind speeds at 4 m s^{-1} linearly increasing to 70 at 7 m s^{-1} and again linearly decreasing to 10 cases at 14 m s^{-1}. For higher wind speeds, the number of measurements decrease linearly to three cases at 20 m s^{-1}. When comparing the statistics for the blade flap root, a fine agreement is seen between measurements and simulations in the free and wake sectors. Further it is seen that the wake only impacts the mean and minimum loads in terms of a decrease, whereas the maximum loads remain unchanged. As for the fatigue loads, generally a good agreement is seen between measurements and simulations in both free and wake sectors. A good agreement is also seen for the statistics of the yaw moment in the wake sector. The increase in max–min loads between free and wake sectors is also clearly seen when comparing Figures 11 and 13. The measurements indicate even larger load than simulated at 13–14 m s^{-1}, which is also reflected in the fatigue load results. A good agreement is seen for the statistics of the tower loads, whereas the agreement between simulation and measurements is not impressive for the fatigue loads of the tower. Somehow it seems that the simulated efficient damping of the tower is too large in the simulations even though the structural damping is only a logarithmic decrement of 1%. The explanation may be a combination of small differences in the controller, time constants in the dynamic inflow model or perhaps length scale of the ambient turbulence. The increase in fatigue loads of the tower from free to wake sector is approximately a factor of 2, which is seen in both measurements and simulations. It should be noted that the accuracy of the predictions—measured in terms of statistics as well as fatigue loads—is of the same order of magnitude for the free sector and the wake sector.

Finally, the comparison of power curves is shown in Figure 14 for both free and wake sectors. It is seen that the DWM model is capable of a very accurate prediction of the 7*D* wake condition for the WT7 turbine located as the sixth turbine in the row. This clearly demonstrates that the DWM approach is good and fully mature toward detailed power predictions of wind turbines in wind farms.

3. WAKE LOADS AS FUNCTION OF WIND DIRECTION

For mean wind speeds between 7.5 and 8.5 m s^{-1}, loads have been extracted from the measurement database as function of wind direction. Since there is only one met mast, the wind speed and the wind direction can unfortunately not be used for all directions. Therefore, wind directions have been derived on the basis of turbine orientation, and wind speeds were based on electrical power productions of turbines in free inflow conditions. The simulated loads on WT7 have been compared with measurements for all wind directions at 8 m s^{-1} in Figure 15 showing the equivalent fatigue load level and electrical power production, respectively. The wind direction polar 0°–360° is covered with a resolution of 2°, each consisting of three half-hour simulations with different speeds for the turbulence generation. When comparing the fatigue loads for all

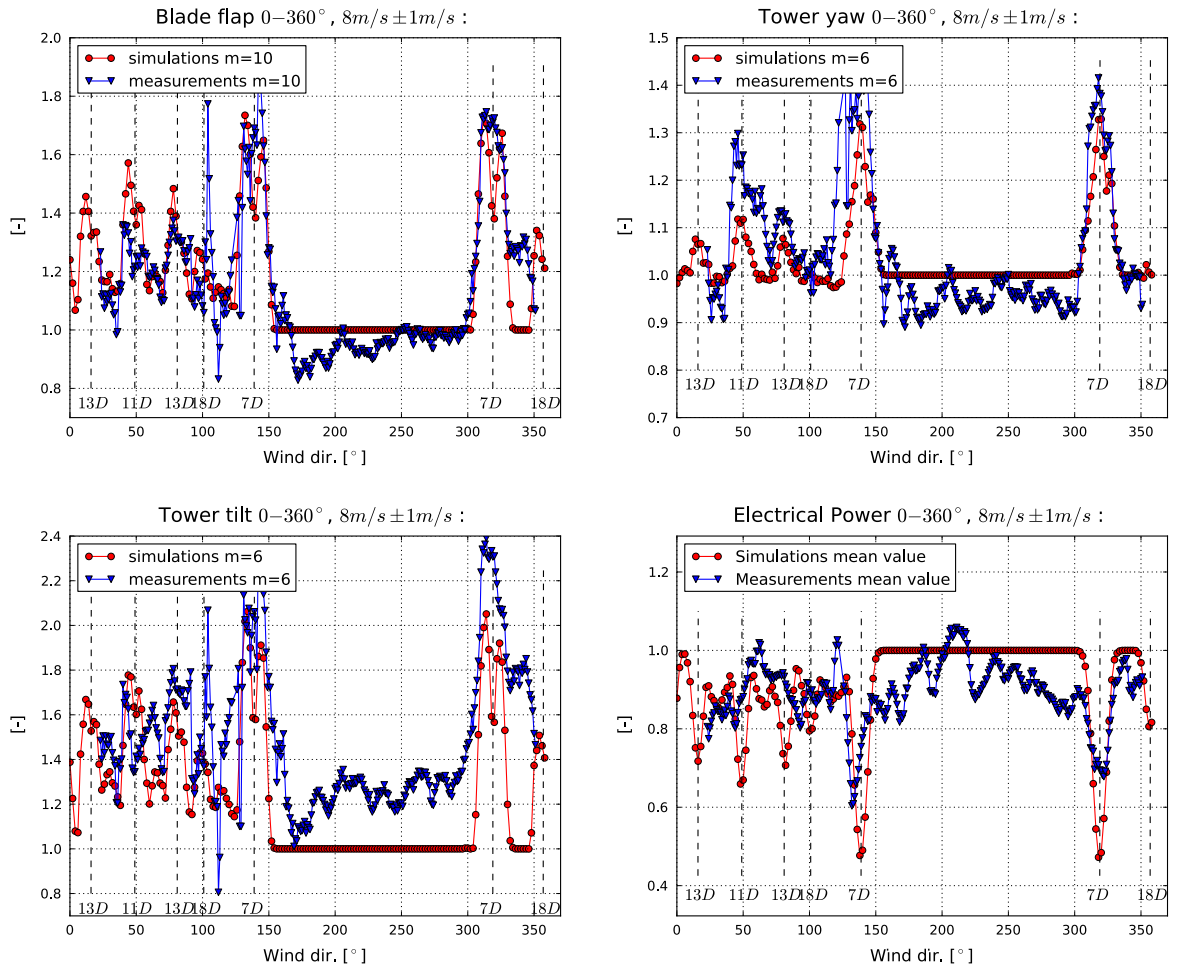

Figure 15. Equivalent fatigue loads of selected moment signals as well as electrical power production as function of wind direction in the Egmond aan Zee wind farm. The wind speed is 8 m s^{-1} at 6% ambient turbulence intensity. Results are non-dimensioned with the simulation result in the free sector. The vertical lines are used to illustrate the distance to the closest upstream turbine at the specific wind direction.

wind directions, a very good agreement regarding both the wind direction for load increase as well as the absolute level of loads is observed. The load increase is observed for row spacings not only at $7D$, but also at $11D$ and $13D$. Even at $18D$, small effects are seen, but these peaks seem to be of magnitude in size of the general uncertainty level observed in the free sector.

4. WIND FARM PRODUCTION AS FUNCTION OF WIND DIRECTION

Two sets of comparisons have been performed for the full 0°–360° direction polar. First, simulated and measured total farm power have been compared. The simulations were performed with a modified version of HAWC2 only including aerodynamics and a rigid rotor in order to reduce the simulation time. With this code, a 10 min simulation takes approximately 1 min on a 3 GHz PC. The turbine controller is fully implemented. Simulations covering the 0°–360° polar with a resolution of 2° for each of the 36 turbines including wake effects of all surrounding turbines have been compared with measurements in Figure 16. Each point in the measurements represents a wind sector of 5°. Therefore, the simulations are presented in two ways. First, the raw results are shown. Secondly, a filtered data set is shown. This filter consists of a simple window averaging of the direction observed and the neighboring points, thus corresponding to a wind sector of 5°. Clear power drops are seen in both measurements and simulations for the wind direction along the rows with $7D$ and $11D$ separation, respectively. Effects attributed to $13D$ spacing can also be seen in the simulations, where this is more unclear in the measurements. In general, a very good agreement is seen, which indicates the potential for using the DWM approach for wind farm production estimates too. Differences in the power level can be seen for $7D$ spacings, where the simulation model

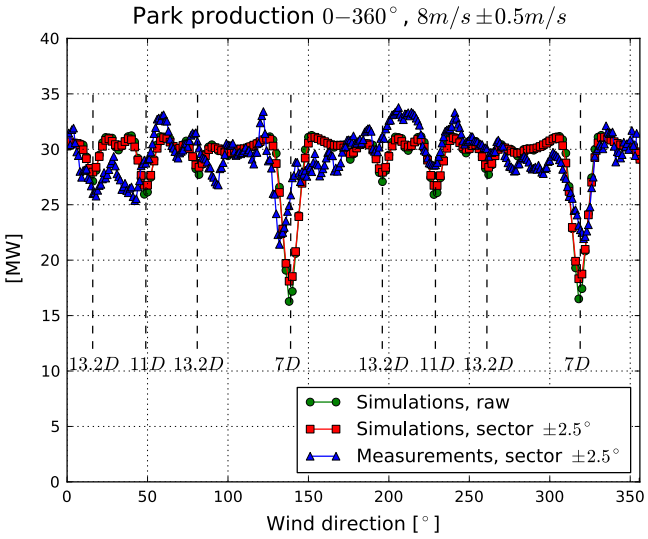

Figure 16. Total wind farm power production in the Egmond aan Zee wind farm at 8 ± 1 m s^{-1}. Simulations are performed using an ambient turbulence level of 6%. The vertical lines are used to illustrate the distance to the closest upstream turbine at the specific wind direction.

results in higher power reductions than shown in the measurements. Clearly this is a complicated load case, but a probable cause could be inaccuracies in determining the representative wind direction with a one-point observation for the full park, which has a spatial extent of up to 7 km. Since the level of power drops in general is highly sensitive to the level of free, half and full wake operation state, small errors in wind direction could have a large smoothing effect in this measurement presentation. Another error source might relate to the fact that we, for a given mean wind direction, assume a stationary stochastic turbulence process in the turbulence model used, whereas real life turbulence is instationary. The instationary part introduces direction trends and could also cause the wind direction far from the met mast to have a different mean value than assumed. A third aspect relates to the target spectra for the turbulence model, which is based on sub-inertial range only and originally fitted for 10 min periods. If the energy content in the applied model is too low on the large scales, the meandering could be slightly underestimated causing a slightly conservative result. Finally, small differences in ambient turbulence intensity between measurements and simulation will cause differences in the power levels.

5. CONCLUSIONS

The DWM model implemented in the aeroelastic code HAWC2 has been extended for handling multiple wakes including handling of wake meandering of multiple wakes. The model has been validated on the basis of the comparisons of model predictions with full-scale turbine measurements from the Dutch wind farm Egmond aan Zee consisting of 36 Vestas V90 turbines. One turbine, located as the sixth turbine in a row, is fully instrumented with load sensors recording blade bending moments, tower bending moments and tower torsion moments as well as operation sensors recording rotor speed, pitch angle and electrical power output. The measurements are of a remarkable high quality enabling comparison of not only fatigue loads, but also simple statistics in terms of maximum, minimum and mean values. When comparing the predicted power curves with measurements in both free and wake sectors, an excellent agreement is seen. A very fine agreement is also seen between measured and simulated loads in both free sector and a sector with wake effects from five turbines separated with seven diameters. The load predictions were shown to match measurements for all signals investigated (blade, yaw and tower moments) in terms of both statistical measures and fatigue equivalent moments. The conclusion of this paper is twofold. First, this paper serves as a general validation of the HAWC2 aeroelastic model as a valid tool for simulating wind turbine load response in the time domain. Second, the DWM model complex is validated in detail for a complex wake situation deep inside a row of turbines. It is shown/demonstrated that the DWM model can be used to obtain reliable predictions of both power output and loads and that many details seen in the measurements are also captured by the model. Wake meandering as a stochastic flow phenomenon caused by large-scale ambient turbulence has previously been recognized on the basis of analyses of detailed full-scale field experiments[17] as well as analyses of detailed boundary layer wind tunnel experiments.[41,42] The model of the wake meandering behavior is a very essential part of the DWM model, where it is responsible for the increased intermittent turbulence on frequency scales that cause large impacts on wind turbine

structures[16]. Since the match between the simulations and full-scale measurements for the analyzed complicated wake case is as good as for the investigated free inflow case, the present work enables the conclusion that wake meandering, caused by ambient turbulence, is indeed an important contribution to the complex wake flow in wind farms. Especially the tower loads would not experience any significant load increase, if it was not for the wake meandering causing variations in the load pattern over the full rotor. Another strong evidence of the DWM model's ability to capture the essential flow field characteristics is obtained from the maximum loads of the blades. These do not increase significantly in wake situations, which is due to the reduced wind speed in the wakes always being lower than the ambient wind. The DWM model is now at a mature level and can be considered ready for industrial applications.

ACKNOWLEDGEMENTS

The work has been funded by the European Commission in the Framework of the Non-Nuclear Energy Programme Sixth Framework under the contract no. REN07/FP6EN/S07.73680/038641 (TOPFARM—Next Generation Design Tool for Optimization of Wind Farm Topology and Operation). Vestas Wind Systems are acknowledged for the permission to use and publish the measurements, and the Danish PSO Project 'Wake affected offshore tower and foundation loads' under contract 2010-1-10546 is also acknowledged for funding the final part of preparing this paper.

REFERENCES

1. Vølund P. Loads on a horizontal axis wind turbine operating in wake. *Journal of Wind Engineering and Industrial Aerodynamics* 1992; **39**: 317–328.
2. Frandsen S, Chacòn L, Crespo A, Enevoldsen P, Gómez-Elvira R, Hernàndez J, Højstrup J, Manuel F, Thomsen K, Sørensen P. Measurements on and modelling of offshore wind farms. *Technical Report Risø-R-903(EN)*, Risø National Laboratory Denmark, 2009.
3. Christiansen M, Hasager C. Using airborne and satellite SAR for wake mapping offshore. *Wind Energy* 2006; **9**: 437–455. DOI: 10.1002/we.192.
4. Cleve J, Greiner M, Enevoldsen P, Birkemose B, Jensen L. Model-based analysis of wake-flow data in the Nysted offshore wind farm. *Wind Energy* 2009; **12**: 125–135. DOI: 10.1002/we.314.
5. Barthelmie R, Frandsen SF, Nielsen M, Pryor S, Rethore P, Jørgensen H. Modelling and measurements of power losses and turbulence intensity in wind turbine wakes at Middelgrunden offshore wind farm. *Wind Energy* 2007; **10**: 517–528. DOI: 10.1002/we.238.
6. Barthelmie R, Jensen L. Evaluation of wind farm efficiency and wind turbine wakes at the Nysted offshore wind farm. *Wind Energy* 2010; **13**: 573–586. DOI: 10.1002/we.408.
7. Jensen N. A note on wind generator interaction. *Technical Report Risø-M-2411(EN)*, Risøe National Laboratory, 1983.
8. Ainslie JF. Calculating the flowfield in the wake of wind turbines. *Journal of Wind Engineering and Industrial Aerodynamics* 1988; **27**: 213–224.
9. Quarton D, Ainslie J. Turbulence in wind turbine wakes. *Wind Engineering* 1989; **14**(1): 15–23.
10. Frandsen S. Turbulence and turbulence-generated structural loading in wind turbine clusters. *Technical Report Risø-R-1188(EN)*, Risø-DTU, 2005.
11. Baker RW, Stel NW. Wake measurements behind a large horizontal axis wind turbine generator. *Solar Energy* 1984; **33**: 5–12.
12. Troldborg N, Sørensen JN, Mikkelsen R. Numerical simulations of wake characteristics of a wind turbine in uniform inflow. *Wind Energy* 2010; **13**: 86–99.
13. Jiminez A, Crespo A, Migoya E, Garcia J. Large-eddy simulation of spectral coherence in a wind turbine wake. *Environ. Res. Lett.* 2008; **3**. DOI: 10.1088/1748-9326/3/1/015004. IOP Publishing.
14. Vermeer L, Sørensen J, Crespo A. Wind turbine wake aerodynamics. *Progress in Aerospace Sciences* 2003; **39**: 467–510. DOI: 10.1016/S0376-0421(03)00078-2.
15. Madsen HA, Larsen GC, Thomsen K. Wake flow characteristics in low ambient turbulence conditions, *Proceedings of the Copenhagen Offshore Wind*, Copenhagen, 2005. On CD-rom. www.ewea.org.
16. Madsen HA, Larsen GC, Larsen TJ, Troldborg N. Calibration and validation of the dynamic wake meandering model for implementation in an aeroelastic code. *Journal of Solar Energy Engineering* 2010; **132**(4): 041014-1–041014-14. DOI: 10.1115/1.4002555.

17. Bingöl F, Mann J, Larsen GC. Light detection and ranging measurements of wake dynamics. Part I: one-dimensional scanning. *Wind Energy* 2010; **13**(1): 51–61.
18. Trujillo J, Bingöl F, Larsen GC, Mann J. Light detection and ranging measurements on wake dynamics. *Wind Energy* 2011; **14**: 61–75.
19. Thomsen K, Madsen HA. A new simulation method for turbines in wake-applied to extreme response during operation. *Wind Energy* 2005; **8**: 35–47. DOI: 10.1002/we.130.
20. Thomsen K, Madsen HA, Larsen GC, Larsen TJ. Comparison of methods for load simulation for wind turbines operating in wake. *Journal of Physics: Conference Series* 2007; **75**. DOI: 10.1088/1742-6596/75/1/012072. IOP Publishing.
21. Larsen TJ, Hansen A. How to HAWC2, the users manual. *Technical Report Risø-R-1597(en)*, Risoe National Laboratory, Technical University of Denmark, 2007.
22. Shabana A. *Dynamics of Multibody Systems*. Cambridge University Press: New York, 1998.
23. Hansen MH, Gaunaa M, Madsen H. A Beddoes-Leishman type dynamic stall model in state-space and indicial formulations. *Technical Report Risø-R-1354(EN)*, Risoe National Laboratory, 2004.
24. Leishman J, Beddoes T. A generalized model for airfoil unsteady aerodynamic behaviour and dynamic stall using the indicial method, *Proceeding of the 42nd Annual Forum of the American Helicopter Society*, Washington D.C., 1986; 243–265.
25. Theodorsen T. General theory of aerodynamic instability and the mechanism of flutter. *NACA Report 435*, 1935, 413–433.
26. Madsen HA, Riziotis V, Zahle F, Hansen M, Snel H, Grasso LTF, Politis E, Rasmussen F. BEM Blade element momentum modeling of inflow with shear in comparison with advanced model results. *Wind Energy* 2011; **15**(1): 63–81. DOI: 10.1002/we.493.
27. Sørensen N. General purpose flow solver applied to flow over hills. *Technical Report Risø-R-827(EN)*, Risoe National Laboratory, 1995. ph.d. thesis.
28. Mann J. Wind Field Simulation. *Probabilistic Engineering Mechanics* 1998; **13**(4): 269–283. Elsevier Science.
29. Larsen GC, Madsen HA, Thomsen K, Larsen TJ. Wake meandering—a pragmatic approach. *Wind Energy* 2008; **11**: 377–395.
30. Larsen GC, Madsen HA, Bingöl F, Mann J, Ott S, Sørensen J, Okulov V, Troldborg N, Nielsen M, Thomsen K, Larsen T, Mikkelsen R. Dynamic wake modeling. *Technical Report Risø-R-1607(EN)*, Risoe National Laboratory, Technical University of Denmark, 2007.
31. Taylor G. The spectrum of turbulence. *Proceeding of the Royal Society London A 1938* 1937; **164**: 476–490. DOI: 10.1098/rspa. 1938.0032.
32. Larsen GC, Madsen HA, Troldborg N, Larsen TJ, Réthoré PE, Fuglesang P, Ott S, Mann J, Buhl T, Nielsen M, Markou H, SØrensen JN, Hansen K, Mikkelsen R, Okulov V, Shen WZ, Heath M, King J, McCann G, Sclez W, Carlén I, Ganander H, Migoya E, Crespo A, Jiménez A, Prieto JL, Stidworthy A, Carruthers D, Hunt J, Gray S, Veldkamp D, Mouritzen AS, Jensen L, Krogh T, Schmidt B, Argyriadis K, Froböse P. TOPFARM—next generation design tool for optimisation of wind farm topology and operation. Final report. *Technical Report Risø-R-1805(EN)*, Risoe National Laboratory, Technical University of Denmark, 2011.
33. Schepers J, Obdam T, Prospathopoulos J. Analysis of wake measurements from the ECN wind turbine Test Site Wieringermeer, EWTW. *Wind Energy* 2012; **15**(4): 575–591. DOI: 10.1002/we.488.
34. Hansen KS, Barthelmie RJ, Jensen L, Sommer A. The impact of turbulence intensity and atmospheric stability on power deficits due to wind turbine wakes at Horns Rev wind farm. *Wind Energy* 2012; **15**(1): 183–196. DOI: 10.1002/we.512.
35. OWEZ. Off shore Windfarm Egmond aan Zee, General report. *Technical Report OWEZ_R_141_20080215*, NordzeeWind, 2008. (Available from: www.norzeewind.nl Accessed February 2008).
36. Johansen N. Verification of simulated fatigue loads on wind turbines operating in wakes. *Technical Report MEK-FM-EP 2009-10*, DTU MEK, 2009. Master thesis.
37. Larsen TJ, Hanson T. A method to avoid negative damped low frequent tower vibrations for a floating, pitch controlled wind turbine. *Journal of Physics: Conference Series* 2007; **75**. DOI: 10.1088/1742-6596/75/1/012073. IOP Publishing.
38. Hansen MH, Hansen A, Larsen T, Øye S, Sørensen P, Fuglsang P. Control design for a pitch-regulated, variable speed wind turbine. *Technical Report Risø-R-1500(EN)*, Risoe National Laboratory, 2005.

39. Matsuishi M, Endo T. Fatigue of metals subjected to varying stress, *Japan Society of Mechanical Engineers*, Fukuoka, Japan, 1968.
40. Dowling N. Fatigue failure predictions for complicated stress-strain histories. *Journal of Materials* 1972; **7**(1): 71–87.
41. España G, Aubrun S, Loyer S, Devinant P. Spatial study of the wake meandering using modeled wind turbines in a wind tunnel. *Wind Energy* 2011; **14**: 923–937.
42. España G, Aubrun S, Loyer S, Devinant P. Wind tunnel study of the wake meandering downstream of a modelled wind turbine as an effect of large scale turbulent eddies. *Journal of Wind Engineering and Industrial Aerodynamics* 2012; **101**: 24–33.

DOI: 10.1002/we